Retrieval of Hurricane Rain Rate From SAR Images Based on Artificial Neural Network

Zhancai Liu , Weihua Ai , Xianbin Zhao, Shensen Hu, Kaijun Ren , Chaogang Guo , Li Wang , and Mengyan Feng

Abstract—Spaceborne synthetic aperture radar (SAR) is gradually being applied to hurricane observation because of its all-weather, high-resolution observation capability. In particular, the retrieval of rain rate using SAR images holds significant scientific and practical importance. However, accurately retrieving rain rate over the sea surface, particularly for high rain rate events under hurricane conditions, remains a significant challenge. The study proposes a new method for rain rate retrieval from hurricane SAR images. We have developed a cascaded feedforward neural network model based on Sentinel-1's double-polarized C-band SAR images of 46 hurricanes to retrieve rain rate under hurricane conditions. In order to overcome the problem of local optimal solution of neural network, the genetic algorithm is employed for optimized model parameter selection. Preliminary results indicate that this approach not only enhances the neural network's iteration speed but also improves its prediction accuracy. Compared with the rain rate of the Stepped-Frequency microwave radiometers, the root mean squared error of retrieved rain rate is 3.05 mm/h and the correlation coefficient is 0.88. Furthermore, we independently verify the rain rate during Hurricane Douglas and compared with global precipitation mission 2-level dual-frequency precipitation radar rain rate product, the results demonstrate that our model can effectively retrieve rain rate in the range of 0–60 mm/h under hurricane conditions. The encouraging results prove the feasibility of the method in SAR rain rate retrieval.

Index Terms—Cascaded feedforward neural network (CFNN), genetic algorithm (GA), rain rate, synthetic aperture radar (SAR).

I. INTRODUCTION

SATELLITE remote sensing technology serves as a crucial mean in the study of precipitation, which can overcome the limitations imposed by geographical position and has the characteristics of wide coverage [1]. Synthetic aperture radar (SAR) has all-day, all-weather, high-resolution ocean monitoring capabilities and provides high-quality data for the study of hurricanes. This technology holds significant potential in the observation of tropical cyclones (TCs) structure, air–sea interactions, rain rate, and wind speed. However, due to the imperfect physical connection model between rain rate and backscattering theory, SAR observations are primarily used for surface feature observation, with fewer studies focusing on rain rate events [2]. High spatial resolution ocean monitoring data is crucial for the accurate assessment of hurricane rain rate and wind speed. Accurate SAR images contribute significantly to the examination of the structural characteristics of TCs and their application in TCs' predictions [3].

SAR has become a spaceborne instrument that can detect and quantify ocean surface information with very high spatial resolution. In fact, SAR can penetrate the atmosphere and clouds, making it an ideal tool for studying extreme weather events such as hurricanes. Its cross-polarized signal and copolarized signal are highly sensitive to sea surface information, which can help to retrieve the rain rate in the hurricane eye and the surrounding ocean surface. If SAR images can be utilized for rain rate retrieval, it would greatly enhance important scientific promotion in the fields of global oceanography, meteorology, and climate science.

With the continuous upgrading of space-borne SAR performance, SAR has been widely used to monitor global hurricane activities due to its high spatial resolution, penetrating capability, and its two-dimensional imaging ability of TC structure, which promotes deeper and wider research on the air-sea boundary of TCs [2], [4], [5]. In the process of using SAR to monitor TCs, the observed normalized radar cross section (NRCS) includes the combined effects of dynamic processes such as wind and rain.

Harrison et al. [6] discovered that the ocean rain rate not only impacts air-sea interactions, but also affects energy exchanges in the remote assessment of hurricanes. Subrahmanyam et al. [7] utilized the C-band doppler weather radar to characterize the spatial and vertical structure of the TC "Ockhi," which provides abundant information for the polarized characteristics of the cyclone structure and aids in a deeper comprehension of the microphysical characteristics of hurricanes. In Xu et al.'s study [8], it is proposed that SAR has a significant impact on the mode and intensity of sea surface rain rate, and its potential capabilities allow for the observation of complex atmospheric events such as hurricanes. By establishing a physical radiative transfer model of sea surface rain rate, SAR images from both C-band and X-band can roughly capture sea surface rain rate [8].

A large number of researches show that rain rate plays a key role in the retrieval of sea surface wind field. Due to the intimate connection between rain rate and wind field, the wind field information and the NRCS of C-band SAR can be used to retrieve the rain rate under hurricane conditions. In

addition, copolarized and cross-polarized NRCS (VV + VH) exhibit considerable potential for studying the TC rain field [8]. Yang et al. [9] demonstrate that precipitation significantly impacts the estimation of wind speed from C-band and Ku-band scatterometers. The sea surface wind speed and rain rate are intricately linked, when studying rain rate, the influence of the wind cannot be overlooked. At low wind speeds, rain rate tends to overestimate wind speed values, while at high wind speeds, it tends to underestimate them. Guo et al. [10] investigated the impact of precipitation-related parameters and phenomena on wind speed retrieval under strong hurricane conditions. They discovered that rain rate resulted in an increase in wind speed retrieval errors, and this upward trend was positively correlated with it. Shao et al. [11] proposed an effective rain cell detection method for SAR images in order to explore the influence of rain rate in the process of dual-polarization SAR images wind field retrieval. Additionally, the rain rate is crucial for the retrieval of sea surface waves. Zhao et al. [12] studied the effect of rain rate on the C-band SAR observation of TCs, they found that rain rate did have an important impact on the retrieval of SAR waves, especially in high rain rate sea conditions.

In addition, there have been advancements in rain rate retrieval based on physical methods. Shao et al. [13] simulated VV-polarized NRCS using the geophysical model function (GMF) CMOD5.N based on dual-polarized channel SAR images and retrieved TC wind speed using VH-polarized images, and an empirical algorithm for SAR rain rate retrieval that considers the influence of the maximum wind speed radius has been proposed. Using the dual-polarized channel SAR images as a foundation, Zhao et al. [14] established a method for extracting the TC rain rate from C-band SAR image by using GMF S1IW.NR and the difference between the observed NRCS and the simulated NRCS in the rainfall unit. However, despite these advancements, there still remain challenges in observing hurricanes and rain rate effectively. The available data samples are limited in size, leading to poor performance of the retrieval results for the TC rain rate in terms of accuracy and precision. To address this issue, further research is needed to develop more advanced techniques and refine existing methods to improve data resolution and enhance the accuracy of TC rain rate extraction.

As machine learning gains widespread application in academia, leveraging its power can significantly impact marine remote sensing image information mining [15]. Colin et al. [16] specifically evaluated whether deep learning methods can solve the joint semantic segmentation of a wide range of ocean processes in SAR ocean images and studied the semantic segmentation of ten meta-ocean processes. Experiments demonstrate that the fully supervised model outperforms all tested weakly supervised algorithms, thereby establishing the feasibility of deep learning in addressing oceanic challenges. Wang et al. [17] utilized a convolutional neural network (CNN) based on the Inception v3 model to identify 10 geophysical phenomena in SAR images including rain rate and selected 320 Sentinel-1 wave mode images for each category, subsequently retrained the pretrained Inception v3 model for classification purposes. Guo et al. [18] utilized the transfer learning method to classify the rain rate level in the SAR images by using the CNN and

combined the rain rate correction model to realize the retrieval of wind speed. This method of combining SAR rain rate level recognition with the rain rate correction method improves the retrieval accuracy of SAR wind speed and offers a potential advancement in SAR retrieval of sea surface wind fields. By collecting SAR data of TCs and utilizing a back propagation (BP) neural network, Mu and Li [19] employed five features of SAR data as input of machine learning model to conduct preliminary rain rate retrieval. The findings suggest that machine learning can be effectively applied in SAR rain rate retrieval.

This article aims to employ a machine learning model to retrieve sea surface rain rate during hurricanes based on SAR images and to control the over-fitting of the model by using the genetic algorithm (GA) optimization method. This approach aims to verify the correlation between the backscatter and other information of SAR images and rain rate, thus offering a novel method for global rain rate retrieval.

The rest of this article is organized as follows. A brief description of the datasets used in the study is presented in Section II. Section III introduces the rain rate retrieval model during hurricane conditions. Section IV gives the rain rate retrieval results and accuracy, as well as the hurricane rain rate retrieval example validation. Finally, Section V concludes the article.

II. DATA AND PREPROCESSING

A. Sentinel-1 Images and Preprocessing

The Sentinel-1 mission belongs to the European Space Agency Copernicus program. It consists of two polar-orbiting satellites (Sentinel-1A and Sentinel-1B). S-1A was launched on 3 April 2014, and S-1B was launched on 25 April 2016. Both of them are equipped with C-band SAR operating at a frequency of 5.405 GHz. They can collect cross-polarized and copolarized image information in a variety of imaging modes. SAR of Sentinel-1 has four unique imaging modes: interferometric wide swath (IW), extra-wide swath (EW), strip-map, and wave. The Sentinel-1's core products are available at levels 0, 1, and 2. In this article, dual-polarized SAR images of the level 1 ground range detected (L1GRD) high-resolution products of IW mode and medium-resolution products of EW mode were used. The bandwidth of the IW mode is 250 km, and the spatial resolution of L1GRDH products in IW mode is approximately 20 m × 22 m. The EW mode provides a large swath width of 400 km, and the spatial resolution of L1GRDM products in EW mode is approximately 93 m × 87 m [20].

B. Stepped Frequency Microwave Radiometer Data and Products

Currently, the primary methods for obtaining rain rate data include rain gauge monitoring, radar monitoring, and remote sensing monitoring [21]. However, the accuracy and range of rain gauges and radar monitoring are limited, and remote sensing struggles to capture hurricane tracks. The SFMR was designed to measure the wind speed and rain rate of hurricanes occurring on the ocean. It is carried onboard the hurricane research aircraft of the NOAA. These aircraft equipped with SFMR can measure

rain rate and wind speed along the trajectory with high temporal resolution [22]. The research aircraft can track and pass through the hurricane, enabling the detection of hurricane shape and internal physical characteristics, which will be beneficial for the machine learning model to retrieve the internal characteristics of the hurricane [23]. In addition, Jiang et al. [22] found that the rain rate observed by SFMR would not be saturated until a very high level compared to other radiometers. The rain rate detected by SFMR is highly correlated with the precipitation of airborne radar, and it has a low error rate, which will be very helpful for detecting high rain rate inside hurricanes. SFMR can provide rain rate and surface wind speed data along the aircraft trajectory with a time resolution of 1 s.

C. Hurricane Track Information – International Best Track Archive for Climate Stewardship

The hurricane trajectory data used in this study is derived from NOAA's International Best Track Archive for Climate Stewardship (IBTrACS). This task counts recent and historical TC data and creates an optimal trajectory data set that can be publicly available, thereby enhancing interagency comparisons. In addition to global data files that contain all storms available in IBTrACS, TC track data is available in several subsets, including the modern satellite observations since 1980, three most recent years of data, and storms active in the last 7 days. IBTrACS are provided in three formats including comma separated variable, network common data format (netCDF), and Shapefiles [24]. The hurricane track data used in this article is in netCDF format since the format is more flexible. The hurricane trajectory data provided by IBTrACS has a high temporal resolution of 2 min, which enables almost real-time tracking of the hurricane's eye location.

D. Global Precipitation Mission Data

Global Precipitation Mission (GPM) is an international co-operation initiated by the National Aeronautics and Space Administration for global rain rate monitoring after TRMM. It carries a dual-frequency precipitation radar (DPR) with operating frequencies of Ku-band (13.6 GHz) and Ka-band (35.5 GHz) channels, respectively. It detects precipitation conditions from 65 °S to 65 °N and is more accurate for weak rain rate and weak snowfall events [25]. The GPM data disclosure product encompasses three levels. This study employs the second-level DPR product to juxtapose it with the retrieved rain rate. Within this product, 49 scanning points are captured simultaneously from beneath the satellite, featuring a spatial resolution of 5 km, a scanning width of 245 km, and a vertical resolution of 250 m.

E. Data Matching

In this article, dual-polarized Sentinel-1 SAR images of 46 hurricanes that occurred in the Eastern Pacific and Atlantic from 2016 to 2022 were collected. Data matching was performed based on the spatial and temporal information of Sentinel-1 SAR and SMFR to obtain hurricane monitoring data. Since SFMR is mounted on the aircraft, there exists a temporal delay between
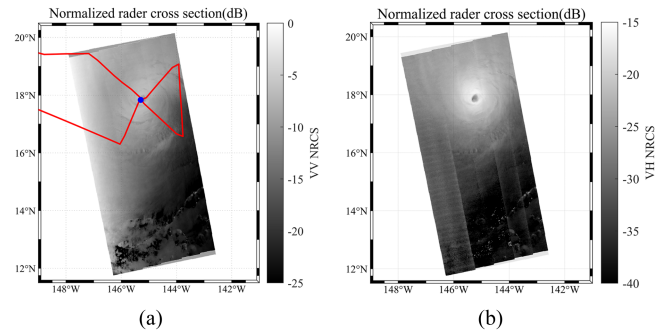

Fig. 1. (a) Quick-look from the VV polarized Sentinel-1 SAR image acquired in EW swath mode over hurricane Douglas at 03:48 UTC on 25 July 2022. (b) Corresponding quick-look of the image in VH polarized. The red line denotes the track of the SFMR onboard the hurricane aircraft.

the real-time monitoring information and SAR images. In order to ensure the accuracy of this study, a time window of 2 h was established for the purpose of matching SAR and SFMR data. In addition, the rain rate data of SFMR were averaged every 20 s. In space, the latitude and longitude correction of SFMR is achieved by utilizing the hurricane's movement speed [26], aiming to enhance the precision of spatial positioning. In this article, wind speed data obtained from SFMR was utilized, and a comparative analysis was conducted between wind speed data provided by the European Centre for Medium-Range Weather Forecasts. The accuracy of SFMR has been established at a high level, making it recognized as true rain rate values.

Fig. 1(a) and (b) depicts the quick-looks of one of the collected images in dual-polarized SAR images from the matching dataset, which were acquired at 03:48 UTC on 25 July 2022 during the period of hurricane Douglas. The red line denotes the track of the NOAA aircraft. The blue point is the hurricane center.

III. RAIN RATE RETRIEVAL MODEL DURING HURRICANE CONDITIONS

The flow chart of rain rate retrieval during hurricane conditions using SAR images based on machine learning method is shown in Fig. 2. The Cascaded feedforward neural network (CFNN) is an artificial neural network that incorporates the error BP algorithm of BP neural network, the input layer of the network is not only connected to the hidden layer, but also directly connected to the output layer, which enhances the relationship between input features and output features, enabling it to perform various tasks including regression and classification. The CFNN's ability to realize nonlinear mappings, coupled with its strong adaptability and error backpropagation process, makes it well-suited for rain rate retrieval based on SAR images. So far, there has not been an established physical model or empirical formula to realize SAR image rain rate retrieval. This model is also suitable for us to obtain the nonlinear relationship between SAR information and marine element information through machine learning methods, without any prior experience information, so it can occupy a place in the field of marine remote sensing. At the same time, GA was used to fine-tune the weights and thresholds of the CFNN, aiming to identify the
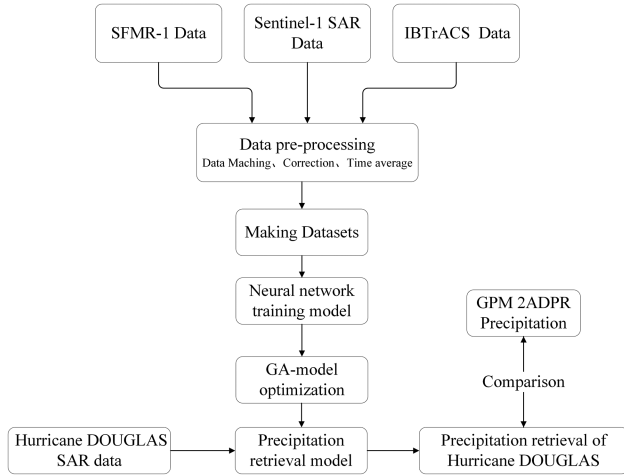
Fig. 2. Flow chart of SAR image rain rate retrieval based on machine learning.
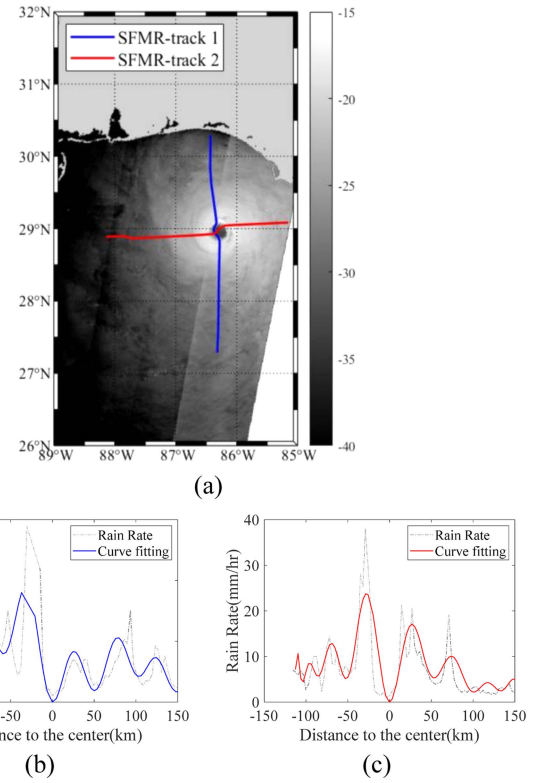

Fig. 3. Variation of rain rate with distance to hurricane center. (a) Quick-look from the VH polarized Sentinel-1 SAR image over hurricane Michael at 11:49 UTC on 10 October 2018. The blue and red lines denote the track of the SFMR. (b) Rain rate of the blue track. (c) Rain rate of the red track.

optimal solution, so as to address the neural network's propensity to converge to a local optimal value, thereby enhancing its performance.

A. Model Training Features

After selecting the machine learning training model, it is essential to control the input and output of the model. The output feature is obviously the rain rate surrounding hurricanes. At this point, the selection of input features is very important to ensure accurate output results. To establish a stronger connection between input features and rain rate, meticulous consideration of the model's input is essential. According to Shao et al. [11], it is known that VV-polarized NRCS (σ_0^{VV}) and VH-polarized NRCS (σ_0^{VH}) hold significant importance in rain rate retrieval from SAR images. Although the incident angle may not be directly linked to the rain rate, it remains a crucial parameter for SAR echo observation. Furthermore, the rain rate has a very obvious effect on wind field retrieval [12], rain rate affects both NRCS and wind speed retrieval, many scholars have identified a correlation between rain rate and wind speed in hurricanes, included as an input feature in the model.

In addition, from the hurricane data, there is almost no rainfall in the hurricane center, and as the distance from the center increases, the rain rate first reaches a peak and then decreases. Fig. 3. presents the connection between the rain rate, as measured by SFMR, and the distance from the hurricane's center. Two paths passing through the hurricane's center were chosen to visualize the relationship, which are represented in Fig. 3(a). Notably, Fig. 3(b) and (c) indicates that at the hurricane's center, the rain rate is zero. As the distance increases, the rain rate initially rises, then exhibits regular oscillation, and ultimately generally exhibits a descending trend. Therefore, it is evident that the amount of rainfall is somewhat connected to the distance from the hurricane center.

As was mentioned by Wang et al. [17], incorporating latitude information as a geographical parameter can better represent hurricane formation, which is conducive to the retrieval of rain rate.

The σ_0^{VV}, σ_0^{VH}, incident angle (θ), and latitude (φ) are used as the basic inputs of the model, and then the distance parameter (D) and wind speed (v) are added as additional input features to evaluate the correlation and error of the model retrieval rain rate after different features are added. This evaluation aids in understanding the impact of input parameters on the model's performance and identifies the most practical feature inputs.

B. Cascaded-Feedforward Neural Network Settings

The Cascaded-Feedforward Neural Network (CFNN) is improved on the basis of feedforward neural network, which has strong fault tolerance. In the event of neuron damage, that is, when neurons in a specific region or layer in the artificial neural network have abnormal function or damage due to data problems or training problems, the output value or weight value of neurons is abnormal or faulty, it minimizes impact on the overall network [27], [28]. The information of network memory is stored on the connection weights between neurons, which is a distributed storage method. The learning function is powerful, enabling the acquisition of connection weights and structures through learning. In comparison to the BP neural network, CFNN combines both backpropagation and cascade-correlation algorithms. Each layer within the CFNN is connected with the input layer cross-layer, which is a fully connected neural network. This increased connectivity boosts the neural network's training speed [29] and enhances its nonlinear fitting capabilities.

The output vectors of each layer of the CFNN with multiple hidden layers are as

$$Y_n = f_n \left(W_1^n \times Y_{n-1} + W_2^n \times p + B_n \right) \qquad (1)$$

where n is the number of neural network layer, Y_n is the output vector, f_n is the neural network activation function, W is the weight function of the hidden layer, B is the bias of the hidden layer, the rows of W or B is the number of neurons in each layer, the columns are the number of input individuals, and p is the input vector.

Mathematical theory proves that a three-layer neural network can approximate any nonlinear continuous function with arbitrary accuracy [30], [31]. The structure of CFNN consists of the input layer, the hidden layer, and the output layer. The number of neurons in the input and output layers is determined by the specific inputs and outputs of the model under consideration. The number of neurons in each layer plays a crucial role in determining the model's applicability and accuracy. Deeper hidden layers theoretically enhance the model's ability to fit functions. However, in practice, deeper layers may lead to overfitting issues and increase training difficulty, making it challenging for the model to converge. After meticulous adjustments, it is reasonable to set the number of the input layer, the hidden layer, and the output layer to 1, 3, and 1, respectively, [19]. Furthermore, if the number of neurons in the hidden layer is insufficient, the neural network lacks the necessary learning and information-processing abilities. Conversely, an excessive number of hidden layer neurons not only significantly increases the complexity of the network structure but also makes the network more likely to get trapped in local minima during the learning process, thereby slowing down the learning speed. This article combines empirical rules with minimum error to determine the number of hidden layer neurons. When the number of neurons reaches the optimal value, the model's error is minimized. Since the performance of the network training is influenced by random initialization, the model undergoes 500 training iterations for each value of the neuron count, resulting in a histogram of neuron frequencies that initially increases and then decreases. The steps are as follows.

Step1: According to the empirical formula (2), the range of values for the number of neurons in the ith layer is determined as $[N_{\min}, N_{\max}]$. Please note that for other hidden layers with unknown number of neurons, the number of neurons is set to 1, indicating a direct linear relationship with the output layer

$$N_h = \sqrt{N_x + N_y} + a \qquad (2)$$

where N_h denotes the number of neurons in the hidden layer, N_x represents the number of neurons in the previous layer, N_y represents the number of neurons in the next layer, and a is a constant where $a \in [2, 10]$ and $a \in N_+$.

Step2: Set the number of neurons in the ith hidden layer to N_{h_i} where $N_{h_i} \in [N_{\min}, N_{\max}]$ and $N_{h_i} \in N_+$. For each N_{h_i}, we train 500 times and obtain the root mean square error for comparison.

Step3: The number of neurons in the ith hidden layer is set to $N_{h_i}^0$, which represents the value with the highest frequency

TABLE I
RESULTS OF CALCULATION OF THE NUMBER OF NEURONS IN THE HIDDEN LAYER

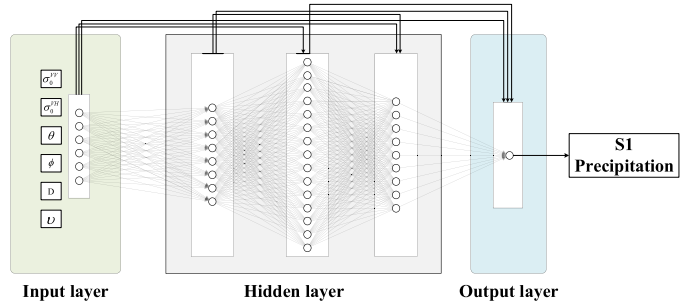| Hidden layer	$[N_{min}, N_{max}]$	$N_{h_i}^0$
1	[5], [14]	8
2	[4], [17]	15
3	[6], [14]	9

Fig. 4. Structure of CFNN model for hurricane rain rate retrieval. ("S1 precipitation" represents the retrieved rain rate from Sentinel-1 SAR images).

of occurrence when the root mean square error is minimized. Proceed to **Step 1**.

Step4: If the frequency of neuron numbers varies monotonically, then the optimal value does not lie within the interval $[N_{\min}, N_{\max}]$, and it is necessary to expand the range of values. Based on the Hecht–Nelson formula [32] and the Lawrence–Fredrickson formula [33], to further determine the range of neuron quantities, proceed to **Step 2**

$$\min \left(\frac{N_x + N_y}{2}, 2N_x + 1 \right) \leq N_h$$

$$\leq \max \left(\frac{N_x + N_y}{2}, 2N_x + 1 \right). \qquad (3)$$

Finally, the number of neurons in the three hidden layers is set to 8, 15, and 9, as shown in Table I, respectively, yielding the best-retrieved results for the model. The overall structure of the CFNN model designed in this article is shown in Fig. 4.

According to the structure of CFNN, we obtain the output of each hidden layer as

$$y_1^i = f_1 \left(\sum_{i=1}^{N_1} W_1^i x_i + B_1^i \right) \qquad (4)$$

$$y_2^j = f_2 \left(\sum_{i=1}^{N_2} W_2^i y_1^i + \sum_{j=1}^{N_1} W_{1,j} x_j + B_2^j \right) \qquad (5)$$

$$y_3^k = f_3 \left(\sum_{i=1}^{N_3} W_3^i y_2^j + \sum_{k=1}^{N_1} W_{1,k} x_k + B_3^k \right) \qquad (6)$$

where $y_n^{i,j,k}$ is the output of the neuron (i, j, k) in the hidden layer n (n is 1, 2, or 3), f_n is the activation function of the hidden layer n, x is the input of neural network. N_n is the number of neurons in the upper layer of the hidden layer n (N_1 is the number

of neurons in the input layer). W_n^i is the connection weight between the hidden layer n and the upper layer's node. $B_n^{i,j,k}$ is the offset of the neuron (i, j, k) in the hidden layer n. $W_1^{i,j,k}$ is the connection weight from the neural network input layer to the corresponding hidden layer (i, j, k).

The selection of transfer function of the hidden layer and the output layer has an important influence on neural network's retrieval accuracy. The transfer function makes the neural network have nonlinear mapping ability. For the transfer function selection of the model, there are generally *purelin*, *tan-sigmoid*, *log-sigmoid*, etc.

The linear transfer function (*purelin*) does not change the linearity of the map, the input is equal to the output, and n is the input

$$\text{purelin}(n) = n. \tag{7}$$

The logarithmic nonlinear mapping transfer function (*log-sigmoid*) enables the output to be mapped to the input to a value between 0 and 1 according to the logarithmic function:

$$\text{logsig}(n) = \frac{1}{1 + e^{-n}}. \tag{8}$$

The hyperbolic tangent nonlinear mapping transfer function (*tan-sigmoid*) enables the output to be mapped the input to a value between -1 and 1 according to the hyperbolic tangent function:

$$\text{tansig}(n) = \frac{e^n - e^{-n}}{e^n + e^{-n}}. \tag{9}$$

It has been demonstrated that when the hidden layer transfer function is set to *tan-sigmoid* and the output layer transfer function is set to *purelin*, adjusting the active interval of the subsequent layer can yield more effective results.

The loss function is employed to assess the discrepancy between the neural network-derived rain rate retrieval and the actual output. The loss function chosen for this analysis was root mean squared error (RMSE)

$$\text{RMSE} = \sqrt{\frac{1}{n} \sum_{i=1}^{n} (p_i - \overline{p_i})^2} \tag{10}$$

where $\overline{p_i}$ is the rain rate detected by the SFMR, p_i represents the rain rate from model retrieval, and n is the total number of samples.

The input data of the model were randomly divided into training, validation, and test sets. Additionally, an SAR image was reserved as an independent test set of the model to better show the universality of the model. The reserved image was hurricane Douglas occurred in the northeastern Pacific Ocean on 25 July 2022. After data matching, a total of 14 046 juxtaposed data samples from dual-polarized Sentinel-1 SAR images and simultaneously measured by SFMR data of 46 hurricanes were collected in the study. These samples were then divided into training set, validation set, and test set at a ratio of 7:2:1.

C. Optimization of CFNN Based on GA

GA is an optimization algorithm based on evolutionary theory and genetic principles. By simulating biological evolution, it
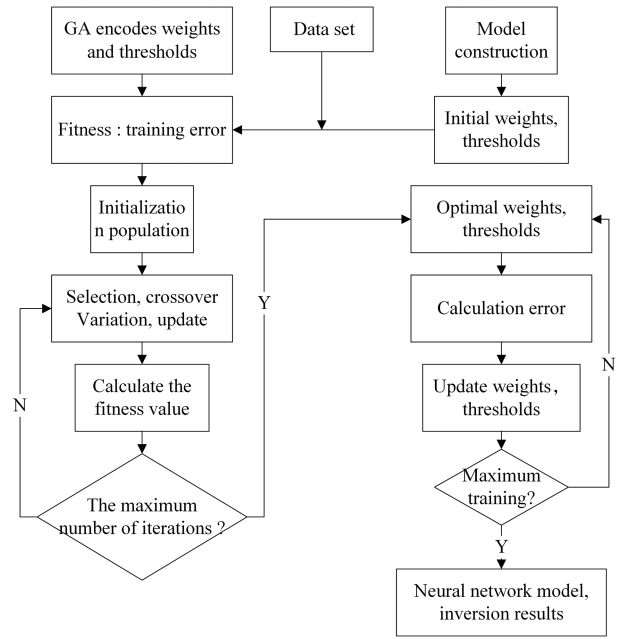

Fig. 5.   Flow chart of CFNN optimization based on GA.

iterates, evolves, and optimizes from an initial population, and finally obtains a relatively better solution. In the field of machine learning, GA has found extensive application in fine-tuning parameters and optimizing model outputs. The intricate workings of neural networks are particularly sensitive to the weights and thresholds assigned to their nodes, and GA can avoid the shortcomings of the initial weight and threshold randomization in the neural network. It is crucial to note that the parameters within the GA algorithm greatly impact its global performance and rate of convergence. The algorithm flow we used is shown in Fig. 5.

The population size is set to 40, the maximum genetic algebra is set to 100, and the crossover probability and mutation probability are predefined constants, typically within the ranges of 0.3–0.8 and 0.001–0.1. In this article, the crossover probability is 0.7 and the mutation probability is 0.01.

IV. RESULTS AND VALIDATION

A. CFNN Neural Network Retrieval of Precipitation

Upon comparison, it was observed that the utilization of wind speed, as well as its absence, significantly impacts the model's retrieval of rain rate. Additionally, this article also delves into the influence of the distance parameter D on the retrieved rain rate. The result is presented in Fig. 6.

Fig. 6 shows the rain rate retrieval effect map with multiple parameters added to the neural network input. Only σ_0^{VV}, σ_0^{VH} θ, and φ are used as input, the RMSE of the training set is 4.23 mm/h, and the correlation coefficient is 0.68, the RMSE of the validation set is 4.55 mm/h, and the correlation coefficient is 0.67.
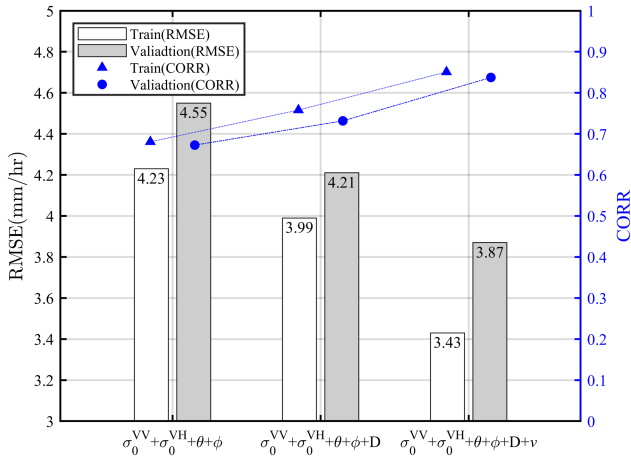
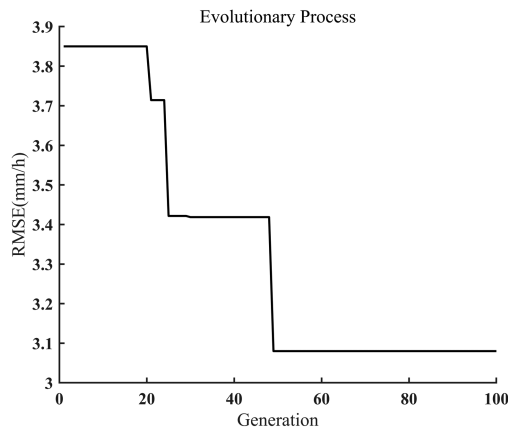Fig. 6. Effect of model retrieval with different features as input.
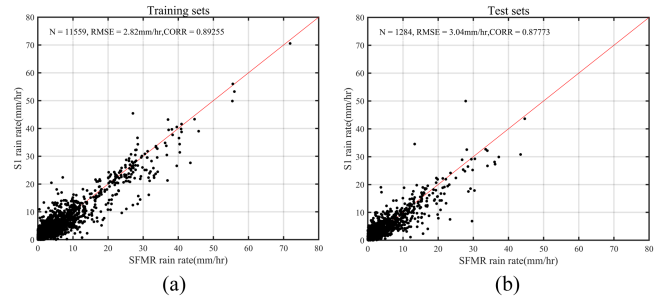

Fig. 7. GA optimization process.

Fig. 8. Comparison of SAR retrieval rain rate and SFMR rain rate. (a) Training sets. (b) Test sets.

49 generations, the neural network tends to converge and the error reaches the minimum target. Fig. 8 shows the comparison between the SFMR rain rate product and the rain rate retrieved using the GA-CFNN model. It is evident that after optimization using the GA, the target expectation is achieved.

After using GA to optimize the neural network, the scatter plot of SAR rain rate retrieval results compared with SFMR rain rate data is shown in Fig. 8. In general, there are more samples with a rain rate of 15 mm/h or less in the training and testing sets and less data with high rain rate, which increases the difficulty of training. After optimization, the RMSE of the training set of the model is reduced to 2.82 mm /h, the correlation coefficient is 0.89. For the test set, the RMSE of the test set is reduced to 3.04 mm /h, and the correlation coefficient is 0.88. It is evident that after GA optimization, the retrieval accuracy of the rain rate has significantly improved.

C. Model Validation

The SAR image of hurricane Douglas occurred in the northeastern Pacific was used for independent verification. It was captured by Sentinel-1 at 03:47 on 25 July, 2020 (UTC), and is independent of the matching data set. This article used GA-CFNN to retrieve the rain rate for it, and the rain rate field around the hurricane eye was obtained. The retrieved rain rate intensity field of hurricane Douglas is shown in Fig. 9. In addition, this article compares the retrieved results with the 2-level DPR rain rate data of GPM, because the rain rate observed by GPM is wider than by SFMR and has two-dimensional structure, which can be better compared with the retrieved rain rate of SAR images. The time information of GPM is 02:30 (UTC) on the same day.

Using the GA-CFNN model, it was retrieved that the maximum rain rate of Hurricane Douglas reached 60 mm/h. Upon comparison, it is found that the results of the retrieved using the method proposed in this article are basically consistent with the GPM rain rate data, but there are a few rainbands that have not been successfully identified. Since the time difference between the SAR image of Hurricane Douglas and the GPM observation is 77 min, the hurricane will move farther away, so it appears that the two hurricanes in Fig. 9(b) and (c) are in different locations. We speculate that these rainbands would move and dissipate over time due to the different times at which the SAR images and GPM data were obtained. In addition, due to the

With the addition of the distance parameter D, the performance of the rain rate retrieval improves. The RMSE of both training set and validation set decreases significantly, and the correlation coefficient is higher than before. When the input parameter v is added, compared to the retrieval effect of only four parameter inputs, the RMSE of the training set and the validation set is reduced by more than 0.7 mm/h, and the correlation coefficient is increased by more than 0.17, which improves the accuracy of the neural network retrieval rain rate. It can be observed that the addition of D and v significantly improves the accuracy of rain rate retrieval results.

In summary, the CFNN model with σ_0^{VV}, σ_0^{VH}, θ, φ, D, and v as input parameters have the best rain rate retrieval level. The RMSE and correlation coefficient of the validation set are 3.43 mm/h and 0.84, respectively.

B. GA-CFNN Model Training

GA is used to optimize the parameters of the neural network. The rain rate retrieval results of GA-CFNN are better aligned with the rain rate true value results obtained from SFMR. Fig. 7 shows the evolution process of GA-CFNN. As can be observed in it that as the genetic algebra increases, when it evolves to
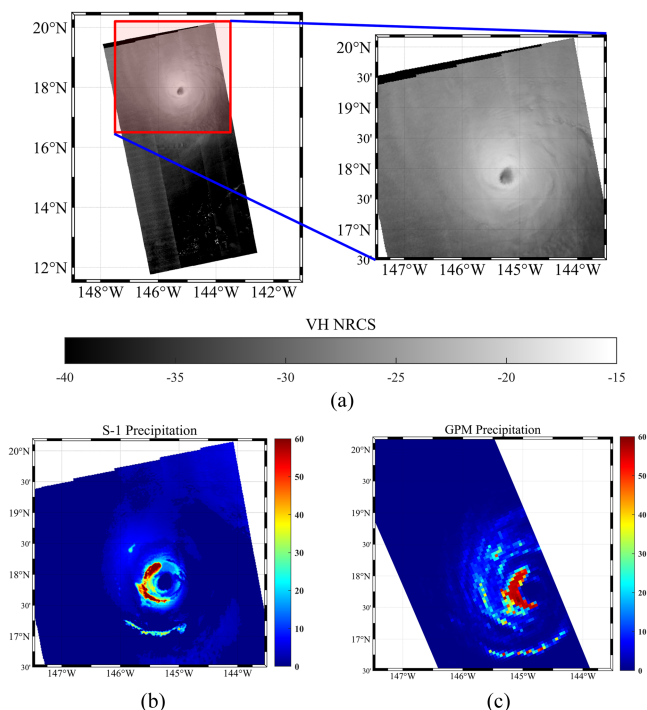
Fig. 9. Comparison of rain rate from SAR image retrieval and GPM rain rate for hurricane Douglas. (a) Quick-look from the VH polarized over hurricane Douglas. (b) Retrieval rain rate of hurricane Douglas. (c) GPM rain rate of hurricane Douglas.

high spatial resolution of SAR, the fine structure of rain rate with high spatial resolution can be obtained, the hurricane rainbands with high rain rate have the same structure as the rain bands of GPM data. Moreover, the high-resolution SAR data allows for the identification of the hurricane eyewall situated between the intense rain band and the eye of the hurricane. In summary, the method outlined in this article is well-suited for retrieving rain rate information surrounding Hurricane Douglas, offering the potential to enhance the accuracy of rain rate retrieval for hurricanes.

V. CONCLUSION

Extreme weather processes, such as hurricanes, have a significant impact on human life. Hurricanes are often accompanied by natural disasters, such as strong winds, rainstorms, and tsunamis, and can even directly affect the safety of human life. Monitoring hurricanes is helpful for taking preventive measures and minimizing losses. Therefore, effective monitoring of hurricanes is of great significance for ensuring human activities.

At present, traditional hurricane monitoring methods rely on aircraft and ground meteorological observations, but these monitoring methods have significant limitations. Therefore, remote sensing has become the primary means of large-scale and all-day ocean monitoring. Although there are some products available for the observation of sea surface rain rate, the retrieval of hurricane rain rate remains a challenge. In addition, due to the limitation in the level and data of hurricane observation, there are errors in the retrieval of hurricane rain rate, making it a significant challenge to improve the accuracy of hurricane

rain rate retrieval. SAR has the ability to obtain all-day, high-resolution hurricane information, and its technology is continuously developing. There is a wealth of global sea data observed by SAR. If SAR can be applied to retrieve rain rate, it will provide an important means for sea precipitation observation and monitoring.

This article proposed a hurricane rain rate retrieval method based on machine learning, particularly GA to optimize neural networks. The SFMR data in the hurricane observation task of the US NOAA program was set as the reference data, achieving favorable rain rate retrieval results. We used the machine learning approach to train the neural network model according to the established data set. This model employed the cross-polarized (VH) and co-polarized (VV) NRCS, incident angle, and latitude information as input to initially verify the feasibility of neural network retrieval of hurricane rain rate. Then, when we add v and D as inputs, the RMSE of hurricane rain rate retrieval is 3.04 and the correlation coefficient is 0.88. To further enhance the accuracy of our results, we used a GA to optimize the neural network's parameters. The rain rate retrieval results of the optimized neural network model exhibited lower errors. When comparing our results with GPM data for hurricane Douglas's rain rate retrieval, we observed good accuracy. This demonstrates the practicality and strength of our approach. It is evident that SAR data can be used to retrieve hurricane rain rate, providing a valuable method for SAR-based rain rate retrieval with significant practical applications.

The article exhibits some limitations. Because the high rain rate in the SFMR observations has a limited number of high rain rate cases, the rain rate is concentrated below 15 mm/h, which increases the difficulty of retrieval and may limit the model's generalizability. Therefore, our next step will focus on developing a method for retrieving rain rate above 15 mm/h. This effort will enhance our understanding of the physical mechanisms involved in extracting rain rate information from SAR images, thereby advancing the field.

REFERENCES

[1] S. Lu, Y. Xie, R. Wang, T. Luo, Z. Xu, and X. Yu, "An algorithm for retrieving the 2-D distribution of moderate rain by X-SAR," *Remote Sens.*, vol. 14, no. 16, Aug. 2022, Art. no. 4081, doi: 10.3390/rs14164081.

[2] Y. Zhao, N. Longépé, A. Mouche, and R. Husson, "Automated rain detection by dual-polarization Sentinel-1 data," *Remote Sens.*, vol. 13, no. 16, Aug. 2021, Art. no. 3155, doi: 10.3390/rs13163155.

[3] G. Zhang, X. Li, W. Perrie, B. Zhang, and L. Wang, "Rain effects on the hurricane observations over the ocean by C-band synthetic aperture radar," *J. Geophysical Res. Oceans*, vol. 121, no. 1, pp. 14–26, Jan. 2016, doi: 10.1002/2015jc011044.

[4] X. Li et al., "Tropical cyclone morphology from spaceborne synthetic aperture radar," *Bull. Amer. Meteorological Soc.*, vol. 94, no. 2, pp. 215–230, Feb. 2013, doi: 10.1175/bams-d-11-00211.1.

[5] Q. Zhang, S. Gong, and L. Lin, "Research on raindrop spectrum inversion based on t-min cumulative rainfall rate time series," in *Proc. Int. Symp. Antennas, Propag. EM Theory*, 2021, pp. 1–3.

[6] E. L. Harrison, F. Veron, D. T. Ho, M. C. Reid, P. Orton, and W. R. McGillis, "Nonlinear interaction between rain and wind induced air water gas exchange," *J. Geophys. Res., Oceans*, vol. 117, no. C3, Mar. 2012, doi: 10.1029/2011jc007693.

[7] K. V. Subrahmanyam and S. R. Baby, "C-band Doppler weather radar observations during the passage of tropical cyclone 'Ockhi'," *Natural Hazards*, vol. 104, no. 3, pp. 2197–2211, Dec. 2020, doi: 10.1007/s11069-020-04268-2.

[8] F. Xu, X. Li, P. Wang, J. Yang, W. G. Pichel, and Y. Q. Jin, "A backscattering model of rainfall over rough sea surface for synthetic aperture radar," *IEEE Trans. Geosci. Remote Sens.*, vol. 53, no. 6, pp. 3042–3054, Jun. 2015, doi: 10.1109/tgrs.2014.2367654.

[9] J. Yang et al., "Effect of precipitation on ocean wind scatterometry," in *Proc. Int. Geosci. Remote Sens. Symp.*, 2004, 7, pp. 4913–4916.

[10] C. Guo, W. Ai, S. Hu, X. Du, and N. Chen, "Effect of precipitation on synthetic aperture radar hurricane wind field retrieval," *Front. Environ. Sci.*, vol. 10, Oct. 2022, Art. no. 1034045, doi: 10.3389/fenvs.2022.1034045.

[11] W. Shao, Z. Lai, F. Nunziata, A. Buono, X. Jiang, and J. Zuo, "Wind field retrieval with rain correction from dual-polarized Sentinel-1 SAR imagery collected during tropical cyclones," *Remote Sens.*, vol. 14, no. 19, Oct. 2022, Art. no. 5006, doi: 10.3390/rs14195006.

[12] X. B. Zhao, W. Z. Shao, L. B. Zhao, Y. Gao, Y. Y. Hu, and X. Z. Yuan, "Impact of rain on wave retrieval from Sentinel-1 synthetic aperture radar images in tropical cyclones," *Adv. Space Res.*, vol. 67, no. 10, pp. 3072–3086, May 2021, doi: 10.1016/j.asr.2021.01.050.

[13] W. Shao, Y. Hu, Z. Lai, Y. Zhang, and X. Jiang, "Rain rate retrieval algorithm for dual-polarized Sentinel-1 SAR in tropical cyclone," *IEEE Geosci. Remote Sens. Lett.*, vol. 20, 2023, Art. no. 4011405, doi: 10.1109/lgrs.2023.3320351.

[14] X. Zhao, W. Shao, Z. Lai, and X. Jiang, "Retrieval of rain rates for tropical cyclones from Sentinel-1 synthetic aperture radar images," *IEEE J. Sel. Topics Appl. Earth Observ. Remote Sens.*, vol. 16, pp. 3187–3197, 2023, doi: 10.1109/jstars.2023.3255922.

[15] X. Li et al., "Deep learning-based information mining from ocean remote sensing imagery," *Nat. Sci. Rev.*, vol. 7, no. 10, pp. 1584–1605, Oct. 2020, doi: 10.1093/nsr/nwaa047.

[16] A. Colin et al., "Semantic segmentation of metoceanic processes using SAR observations and deep learning," *Remote Sens.*, vol. 14, no. 4, Feb. 2022, Art. no. 851, doi: 10.3390/rs14040851.

[17] C. Wang et al., "Automated geophysical classification of Sentinel-1 wave mode SAR images through deep-learning," in *Proc. Int. Geosci. Remote Sens. Symp.*, 2018, pp. 1776–1779.

[18] C. Guo et al., "Correction of sea surface wind speed based on SAR rainfall grade classification using convolutional neural network," *IEEE J. Sel. Topics Appl. Earth Observ. Remote Sens.*, vol. 16, pp. 321–328, 2023, doi: 10.1109/jstars.2022.3224438.

[19] S. Mu and X. Li, "Retrieval of rainfall information by spaceborne C-band SAR based on machine learning," in *Proc. Int. Geosci. Remote Sens. Symp.*, 2022, pp. 4163–4166.

[20] R. Torres et al., "Sentinel-1 system," in *Proc. 10th Eur. Conf. Synthetic Aperture Radar*, 2017, pp. 1582–1585.

[21] A. Battaglia et al., "Research progress on precipitation products of spaceborne precipitation measurement radar," *Rev. Geophys.*, vol. 58, no. 3, Sep. 2020, Art. no. e2019RG000686.

[22] H. Jiang, P. G. Black, E. J. Zipser, F. D. Marks Jr., and E. W. Uhlhorn, "Validation of rain-rate estimation in hurricanes from the stepped frequency microwave radiometer: Algorithm correction and error analysis," *J. Atmos. Sci.*, vol. 63, no. 1, pp. 252–267, Jan. 2006, doi: 10.1175/jas3605.1.

[23] H. Leighton, R. Black, X. Zhang, and F. D. Marks Jr, "The relationship between reflectivity and rainfall rate from rain size distributions observed in hurricanes," *Geophys. Res. Lett.*, vol. 49, no. 23, Dec. 2022, Art. no. e2022GL099332, doi: 10.1029/2022gl099332.

[24] K. R. Knapp, M. C. Kruk, D. H. Levinson, H. J. Diamond, and C. J. Neumann, "The International Best Track Archive for Climate Stewardship," *Bull. Amer. Meteorological Soc.*, vol. 91, no. 3, pp. 363–376, Mar. 2010, doi: 10.1175/2009bams2755.1.

[25] T. Iguchi et al., "An overview of the precipitation retrieval algorithm for the dual-frequency precipitation radar (DPR) on the global precipitation measurement (GPM) mission's core satellite," *Earth Observing Missions Sensors*, vol. 8528, pp. 250–256, Nov. 2012, doi: 10.1117/12.977352.

[26] A. Mouche, B. Chapron, J. Knaff, Y. Zhao, B. Zhang, and C. Combot, "Copolarized and cross-polarized SAR measurements for high-resolution description of major hurricane wind structures: Application to Irma category 5 hurricane," *J. Geophys. Res., Oceans*, vol. 124, no. 6, pp. 3905–3922, Jun. 2019, doi: 10.1029/2019jc015056.

[27] A. M. A. Shohda, M. A. M. Ali, G. Ren, J. G. Kim, and M. A. E. H. Mohamed, "Application of cascade forward backpropagation neural networks for selecting mining methods," *Sustainability*, vol. 14, no. 2, 2022, Art. no. 635, doi: 10.3390/su14020635.

[28] M. Yang, B. Xie, Y. Dou, and G. Xue, "Cascade forward artificial neural network based behavioral predicting approach for the integrated satellite-terrestrial networks," *Mobile Netw. Appl.*, vol. 27, no. 4, pp. 1–9, Jan. 2022, doi: 10.1007/s11036-021-01875-6.

[29] S. A. Rizvi, L.-C. Wang, and N. M. Nasrabadi, "Nonlinear vector prediction using feed-forward neural networks," *IEEE Trans. Image Process.*, vol. 6, no. 10, pp. 1431–1436, Oct. 1997, doi: 10.1109/83.624963.

[30] G. Cybenko, "Approximation by superpositions of a sigmoidal function," *Math. Control Signal Syst.*, vol. 2, no. 4, pp. 303–314, Dec. 1989, doi: 10.1007/bf02551274.

[31] K. Hornik, "Approximation capabilities of multilayer feedforward networks," *Neural Netw.*, vol. 4, no. 2, pp. 251–257, Jan. 1991, doi: 10.1016/0893-6080(91)90009-t.

[32] R. Hecht-Nielsen, "Kolmogorov's mapping neural network existence theorem," in *Proc. Int. Conf. Neural Netw.*, vol. 3, pp. 11–14, Jun. 1987.

[33] S. Karsoliya, "Approximating number of hidden layer neurons in multiple hidden layer BPNN architecture," *Int. J. Eng. Trends Technol.*, vol. 3, no. 6, pp. 714–717, Dec. 2012.

Zhancai Liu received the B.S. degree in marine science, in 2022, from the National University of Defense Technology, Changsha, China, where he is currently working toward the M.S. degree in marine science.

His research interests include ocean remote sensing, radar, and remote sensing techniques and instruments.

Weihua Ai received the B.S., M.S., and Ph.D. degrees in atmosphere science from the PLA University of Science and Technology, Nanjing, China, in 2002, 2004, and 2007, respectively.

He is currently a Professor with the College of Meteorology and Oceanography, National University of Defense Technology, Changsha, China. His research interests include radar simulator and microwave remote sensing.

Xianbin Zhao received the Ph.D. degree in atmosphere science from the PLA University of Science and Technology, Nanjing, China, in 2015.

He is currently the Lecturer with the College of Meteorology and Oceanography, National University of Defense Technology, Changsha, China. He is mainly engaged in the research and teaching of synthetic aperture radar ocean remote sensing. He has authored or coauthored a number of papers in the field of ocean surface wind field and wave retrieval. He is concerned about the impact of precipitation on synthetic aperture radar of ocean sounding.

Shensen Hu received the B.S. degree in radar engineering from the PLA University of Science and Technology, Nanjing, China, in 2014, and the Ph.D. degree in atmospheric science from the National University of Defense Technology, Changsha, China in 2019.

He is currently a Lecturer with the National University of Defense Technology. His research interests include radar meteorology and low-light satellite remote sensing.

Kaijun Ren received the B.S. degree in applied mathematics and the M.S. and Ph.D. degrees in computer science from the National University of Defense Technology, Changsha, China, in 1998, 2003, and 2008, respectively.

He is currently a Professor with the College of Meteorology and Oceanography and the College of Computer, National University of Defense Technology. His current research interests include high performance computing, cloud computing, Big Data, and their interdisciplinary applications in ocean science and meteorology areas.

Chaogang Guo received the B.S. and M.S. degrees in atmospheric science from the National University of Defense Technology, Changsha, China, in 2020 and 2022, respectively.

His research interests include atmospheric physics, radar, and remote sensing techniques and instruments.

Li Wang received the B.S. degree in electronic information engineering and the Ph.D. degree in radio physics from the Wuhan University, Wuhan, China, in 2009 and 2022, respectively.

He is currently a Postdoc with the College of Meteorology and Oceanography, National University of Defense Technology, Changsha, China. His research interests include applications of HF radar currents and tidal and residual currents in the Taiwan Strait.

Mengyan Feng received the B.S. degree in atmosphere science from the Lanzhou University, Lanzhou, China, in 2018, and the M.S. degree in atmosphere science, in 2020, from the National University of Defense Technology, Changsha, China, where he is currently working toward the Ph.D. degree in atmosphere science.

His research interests include satellite-borne microwave radiometer remote sensing and high-frequency radar ocean environment remote sensing, which mainly involves the development of atmosphere and ocean environment retrieval algorithms, signal processing technology, and design of satellite and radar systems.